RSC Advances

PAPER

View Article Online
View Journal | View Issue

Cite this: *RSC Adv.*, 2021, **11**, 7587

Highly crystalline anatase TiO_2 nanocuboids as an efficient photocatalyst for hydrogen generation†

Shubhangi R. Damkale, Sudhir S. Arbuj, Govind G. Umarji, Sunit B. Rane and Bharat B. Kale *

Highly crystalline anatase titanium dioxide (TiO_2) nanocuboids were synthesized *via* a hydrothermal method using ethylenediamine tetraacetic acid as a capping agent. The structural study revealed the nanocrystalline nature of anatase TiO_2 nanocuboids. Morphological study indicates the formation of cuboid shaped particles with thickness of ~5 nm and size in the range of 10–40 nm. The UV-visible absorbance spectra of TiO_2 nanocuboids showed a broad absorption with a tail in the visible-light region which is attributed to the incorporation of nitrogen atoms into the interstitial positions of the TiO_2 lattice as well as the formation of carbonaceous and carbonate species on the surface of TiO_2 nanocuboids. The specific surface areas of prepared TiO_2 nanocuboids were found to be in the range of 85.7–122.9 $m^2\ g^{-1}$. The formation mechanism of the TiO_2 nanocuboids has also been investigated. Furthermore, the photocatalytic activities of the as-prepared TiO_2 nanocuboids were evaluated for H_2 generation *via* water splitting under UV-vis light irradiation and compared with the commercial anatase TiO_2. TiO_2 nanocuboids obtained at 200 °C after 48 h exhibited higher photocatalytic activity (3866.44 μmol h^{-1} g^{-1}) than that of commercial anatase TiO_2 (831.30 μmol h^{-1} g^{-1}). The enhanced photoactivity of TiO_2 nanocuboids may be due to the high specific surface area, good crystallinity, extended light absorption in the visible region and efficient charge separation.

Received 22nd December 2020
Accepted 5th February 2021

DOI: 10.1039/d0ra10750f

rsc.li/rsc-advances

1. Introduction

Titanium dioxide (TiO_2) has attracted tremendous attention in the last few decades due to its potential applications in the field of photocatalysis for solar fuel production and environmental remediation.[1,2] Photocatalytic hydrogen production over semiconductors is an effective and attractive method for the conversion of solar energy to clean and renewable hydrogen fuel.[3–6] Since the first report by Fujishima and Honda in 1972 on the photo-assisted decomposition of water into hydrogen and oxygen using a TiO_2 photoanode in the electrochemical cell,[7,8] extensive research has been carried out to investigate various semiconductor oxides as well as sulphides as photocatalysts for energy and environment related applications.[9,10] Among the reported semiconductor photocatalysts, *viz.* ZnO, TiO_2, SnO_2, Nb_2O_5, CdS and ZnS, TiO_2 is more superior and a benchmark photocatalyst owing to its chemical inertness, appropriate band edge positions, high photostability, low cost and nontoxicity.[1,10–13]

TiO_2 mainly exists in the three different crystalline forms; anatase, rutile and brookite. During the past years, many investigations have confirmed anatase TiO_2 is generally photocatalytically more active than rutile TiO_2 because its larger band gap (3.2 eV) compared to that of rutile (3.0 eV) corresponds to a stronger redox ability.[14] In the crystal structure of anatase, the primary TiO_6 octahedron building units are significantly distorted and interconnected *via* corner and edge sharing to form zigzag chains with a screw axis. Compared with the other two phases, such a structure offers a relatively loose atomic stacking and less density that may be correlated with its greater absorption capability and more abundant active sites (oxygen vacancies).[15] However, the wide band gap of the anatase TiO_2 and the high recombination rate of photogenerated charge carriers have severely restricted the efficiency of TiO_2.[16] Currently, several strategies such as metallic or nonmetallic ion doping[13,16–19] noble metal deposition[20–22] and coupling with other semiconductors[23–25] are developed to extend its photoresponse to visible light or to improve the charge separation. Besides these methods, morphological modification is another adopted method.[26,27] Du *et al.* reported that photocatalytic performance also depends on the exposed facets of TiO_2.[28,29]

The photoactivity of TiO_2 is found to be greatly influenced by a variety of factors including crystalline phase, specific surface area, crystallinity, photon absorption properties and so on.[1,30] Anatase TiO_2 with higher crystallinity is preferred for photocatalysis, since higher crystallinity would mean fewer defects for the recombination of photogenerated electrons and holes.[31]

Centre for Materials for Electronics Technology (C-MET), Off Pashan Road, Panchawati, Pune-411008, Maharashtra, India. E-mail: bbkale1@gmail.com; bbkale@cmet.gov.in; Fax: +912025898180; Tel: +912025899273

† Electronic supplementary information (ESI) available. See DOI: 10.1039/d0ra10750f

Generally, semiconductor based photocatalysis proceeds through following three steps: (1) absorption of light; (2) separation and transport of charge carriers; and (3) redox reactions on the surface of the semiconductor.[32] Since the photocatalytic reactions mainly take place on the surface of photocatalysts, the large surface area is generally favorable to enhance the photocatalytic activity during photocatalysis. Therefore it is crucial to control the particle size as well as morphology of the photocatalyst in order to increase its applicability.[1,33,34] Over the past decades, a variety of controlled synthesis methods such as sol–gel,[35,36] hydrothermal,[37,38] microwave-assisted[39] and chemical vapour deposition[40] have been attempted to synthesize TiO_2 nanostructures with varied morphologies. When compared to the other methods, the hydrothermal method not only enables obtaining materials with a large surface area and high crystallinity but also flexibly adjust the parameters to control the particle size and morphology of products.[41]

So far, numerous morphologies of TiO_2 nanostructures *viz.*, nanowires,[42] nanotubes[43] nanobelts,[44] nanorods,[45,46] nanosheets,[47] nanoflowers,[48,49] hierarchical microspheres[50] have been effectively synthesized by hydrothermal technique. Moreover, many researchers have exploited the synthesized TiO_2 nanostructures for the photocatalytic hydrogen generation. For example, Yu *et al.*[51] have synthesized anatase TiO_2 nanosheets by a simple hydrothermal treatment of the mixed solution of tetrabutyl titanate and hydrofluoric acid which exhibited much higher photocatalytic H_2 production activity than Degussa P25 TiO_2. Flower-like anatase TiO_2 nanosheets fabricated by Jitputti *et al.*[52] using hydrothermal process on amorphous TiO_2 spheres obtained by controlled hydrolysis of titanium isopropoxide in ethanol also showed high photocatalytic activity for H_2 evolution than that of commercial anatase TiO_2 powder after heat treatment. Furthermore, Cheng and co-workers[53] also reported that twinned anatase TiO_2 nanocrystals synthesized by a facile hydrothermal method from hydrolysis of titanium glycolate powder precursor exhibited significantly larger photocatalytic activity towards H_2 production than that of commercial TiO_2 (P25 Degussa). However, many studies have been focused on improving the photocatalytic activity by fabricating TiO_2 with large specific surface area, high crystallinity, enhanced light absorption and so on.

In this regard, herein, we demonstrate a facile synthesis method to prepare highly crystalline 3D TiO_2 nanocuboids having high specific surface area. A titanium precursor was prepared from commercial anatase TiO_2 powder and employed to synthesize TiO_2 nanocuboids *via* a one-pot hydrothermal reaction using EDTA as the capping agent. The hydrothermal reactions were carried out at different time and temperature conditions. The photocatalytic activities of the as prepared TiO_2 nanocuboids were investigated for H_2 generation *via* water splitting and also compared with the commercial anatase TiO_2.

2. Experimental section

2.1. Materials

Commercial titanium dioxide (TiO_2) powder (99.8%, anatase) was purchased from Sigma-Aldrich. Hydrofluoric acid (HF, 40 wt%) was obtained from S. D. Fine Chemicals Ltd, hydrogen peroxide (H_2O_2, 30 wt%), ammonia (NH_3, about 25%) and ethylenediamine tetraacetic acid (EDTA) were all purchased from Fisher Scientific. All the chemicals were used as received without further purification.

2.2. Synthesis of titanium dioxide nanocuboids (TiO_2 NCs)

Commercial TiO_2 powder was employed as the starting material. In a typical synthesis, firstly, 25.0 mmol of TiO_2 powder was dissolved in 25 mL of hydrofluoric acid by heating the mixture in Teflon lined autoclave at 150 °C for 3 h. After cooling the autoclave at room temperature, the reaction mass was again re-precipitated by adding 50 mL of ammonia. The obtained white precipitate was then washed thoroughly with deionized (DI) water to remove excess NH_4^+ and F^- ions. Furthermore, this precipitate was again dissolved in a 60 mL solution containing 50 mL hydrogen peroxide and 10 mL ammonia (5 : 1 by volume) under continuous stirring to get a precursor. To the precursor solution, 12.5 mmol of ethylenediamine tetraacetic acid (EDTA) was added and this mixture was heated at 60 °C for 1 h to promote the decomposition of H_2O_2 and then was transferred into a Teflon-lined stainless steel autoclave. The autoclave was sealed, heated at 200 °C for 24 h and then cooled to room temperature naturally. The resultant precipitate was collected by centrifugation, washed several times with DI water followed by ethanol and dried in an oven at 60 °C overnight. The same procedure was followed to prepare TiO_2 nanocuboids at different reaction time and temperature conditions *i.e.* 48 h, 150 °C; 48 h, 180 °C and 48 h, 200 °C. The obtained TiO_2 nanocuboids were named as TiO_2–NCs 24 h, 200 °C; TiO_2–NCs 48 h, 150 °C; TiO_2–NCs 48 h, 180 °C and TiO_2–NCs 48 h, 200 °C.

2.3. Characterization

X-ray powder diffraction (XRD) patterns were obtained by using a Bruker D8 Advance X-ray powder diffractometer with Cu-Kα radiation in the 2θ range of 20°–80°. The surface morphology of the samples was characterized by field-emission scanning electron microscopy (FESEM, HITACHI S-4800). TEM micrographs were recorded on a field-emission transmission electron microscopy (FETEM, JEOL JEM-2200FS) at an operating voltage of 200 kV. High-resolution TEM (HRTEM) and selected area electron diffraction (SAED) were also recorded on JEOL JEM-2200FS. X-ray photoelectron spectroscopy (XPS) measurement was performed on a Thermo Scientific ESCALAB 250Xi X-ray spectrometer using an Al Kα radiation at 1486.6 eV. Fourier transform infrared (FTIR) spectroscopy measurements were carried out with a Jasco FTIR-6100 spectrometer over a range of 400–4000 cm^{-1}. UV-vis diffuse reflectance spectra were recorded at room temperature in the range 200–800 nm using Shimadzu UV-Vis-NIR spectrophotometer (Model UV-3600). The Brunauer–Emmett–Teller (BET) specific surface areas of the samples were calculated from the N_2 adsorption isotherms at liquid N_2 temperature using Quantachrome NOVA touch LX[1] instrument. The samples were degassed in vacuum at 150 °C for 2 h prior to BET analysis. Photoluminescence (PL) spectra were detected with a Shimadzu RF-5301pc spectroflurophotometer.

The photoconductivity experiments were carried out under solar simulator (Photo Emission Technology, Model: #SS50AAA) integrated with Keithley 4200SCS system.

2.4. Photocatalytic hydrogen generation test

The photocatalytic hydrogen evolution experiments were carried out in a closed reactor system under UV-vis light irradiation using 400 W mercury vapor lamp. The reactor used in the photocatalytic process was a 100 mL cylindrical quartz vessel. The system was well sealed with septum arrangement to remove the evolved gas through gas-tight syringe for quantifying the amount of gases evolved. In a typical photocatalytic experiment, 20 mg of TiO_2 catalyst powder having 1 wt% preloaded platinum as a co-catalyst was suspended in 30 mL solution containing 25 mL deionized water and 5 mL methanol. Before irradiation, the nitrogen gas was bubbled through the reaction mixture in order to remove the dissolved gases. Magnetic stirring of the solution was maintained throughout the experiment in order to keep the photocatalyst particles in suspension status. A 0.5 mL of evolved gas was sampled intermittently through the septum, and hydrogen was analyzed using a gas chromatograph (Shimadzu: Model GC 2014) equipped with 5 Å molecular sieves column. The amount of hydrogen produced was calculated according to the fitted standard curve. Cyclic stability of the most active sample was tested by repeating the photocatalytic reaction three times under identical conditions.

3. Results and discussion

3.1. Structural analysis

Fig. 1 shows the X-ray diffraction patterns of commercial TiO_2 and TiO_2 NCs prepared under different reaction time and temperature conditions. As shown in figure, XRD pattern of commercial TiO_2 shows characteristic diffraction peaks located at $2\theta = 25.3°$, 37.8°, 48.0°, 53.9°, 55.0°, 62.7°, 68.7°, 70.3°, and 75.0° corresponding to the (101), (004), (200), (105), (211), (204), (116), (220) and (215) planes of tetragonal anatase TiO_2 (JCPDS card no. 21–1272), respectively. TiO_2 NCs prepared at different reaction conditions also show similar diffraction patterns with a slight change in the peak position of the (101) plane.

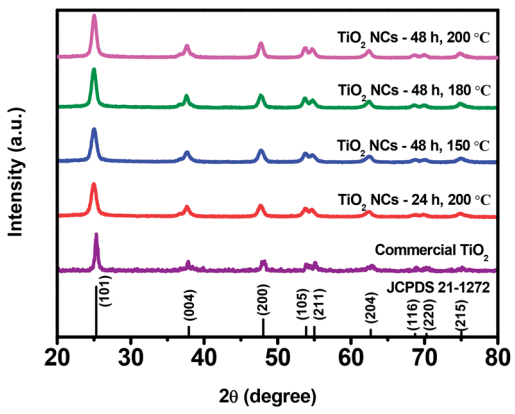

Fig. 1 XRD patterns of commercial TiO_2 and TiO_2 nanocuboids prepared under different reaction time and temperature conditions.

The relatively broad XRD peaks of the as prepared TiO_2 NCs as compared to the commercial TiO_2 sample reveals that the TiO_2 NCs obtained at different reaction conditions have a smaller size. It can be seen that the intensity of the (101) diffraction peak of as prepared TiO_2 NCs increases slightly with increasing hydrothermal reaction time and temperature.

Fig. 2 illustrates magnified (101) peak of commercial TiO_2 and as prepared TiO_2 NCs. As can be seen, a slight shift in the peak position of the (101) plane to lower 2θ value is noticed with all of the as prepared TiO_2 NCs compared to commercial TiO_2 sample. The shift in the 2θ value infers that stress has occurred due to doping of other atoms into the lattice of as prepared TiO_2 NCs and it is discussed in the XPS analysis section.[54]

The average crystallite sizes of the commercial TiO_2 and as prepared TiO_2 NCs were estimated by the Scherrer's formula. The average crystallite size of commercial TiO_2 was found to be 17.3 nm, whereas for TiO_2 NCs prepared under different time and temperature conditions *i.e.* 24 h, 200 °C; 48 h, 150 °C; 48 h, 180 °C and 48 h, 200 °C, the average crystallite sizes were found to be 10.2, 10.3, 11.2 and 11.6 nm, respectively. The relative crystallinity of the as prepared TiO_2 NCs was also quantitatively evaluated *via* the relative intensity of (101) diffraction peak of TiO_2 NCs prepared at 200 °C for 24 h. The relative crystallinity of the TiO_2 samples is listed in Table 1. It was observed that the average crystallite size and relative crystallinity of as prepared TiO_2 NCs increases with increasing reaction time and temperature.

3.2. Morphological analysis

Fig. 3 displays the FESEM images of commercial TiO_2 and as prepared TiO_2 NCs. The commercial TiO_2 powder exhibits irregularly-shaped particles with a size in the range of 50–200 nm (Fig. 3a). However, after hydrothermal treatment under different time and temperature conditions and with EDTA capping, commercial TiO_2 shows a significant morphological transition from irregular large particles to very small sized particles. Since the particle size of as prepared TiO_2 nanostructures is too small, its morphology and size cannot be

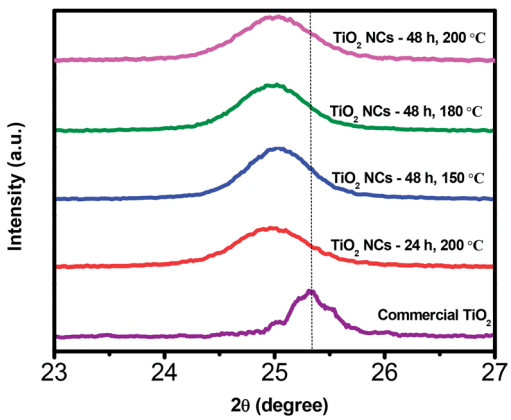

Fig. 2 Magnified XRD patterns of (101) plane of commercial TiO_2 and TiO_2 nanocuboids prepared under different reaction time and temperature conditions.

Table 1 Relative crystallinity, band gap, specific surface area and H_2 generation in μmol h^{-1} g^{-1} of commercial TiO_2 and as prepared TiO_2 nanocuboids

Sample	Relative crystallinity[a]	Band gap (eV)	Specific surface area (m^2 g^{-1})	H_2 generation (μmol h^{-1} g^{-1})
Commercial TiO_2	—	3.27	29.3	831.30
TiO_2–NCs 24 h, 200 °C	1	3.24	122.9	1706.40
TiO_2–NCs 48 h, 150 °C	1.02	3.20	111.6	1924.31
TiO_2–NCs 48 h, 180 °C	1.17	3.16	103.2	2954.78
TiO_2–NCs 48 h, 200 °C	1.28	3.12	85.7	3866.44

[a] Relative crystallinity is calculated using the ratio of intensity of diffraction peak from the (101) plane of anatase TiO_2 NCs prepared under different reaction conditions to the intensity of the (101) peak of TiO_2 NCs prepared for 24 h at 200 °C.

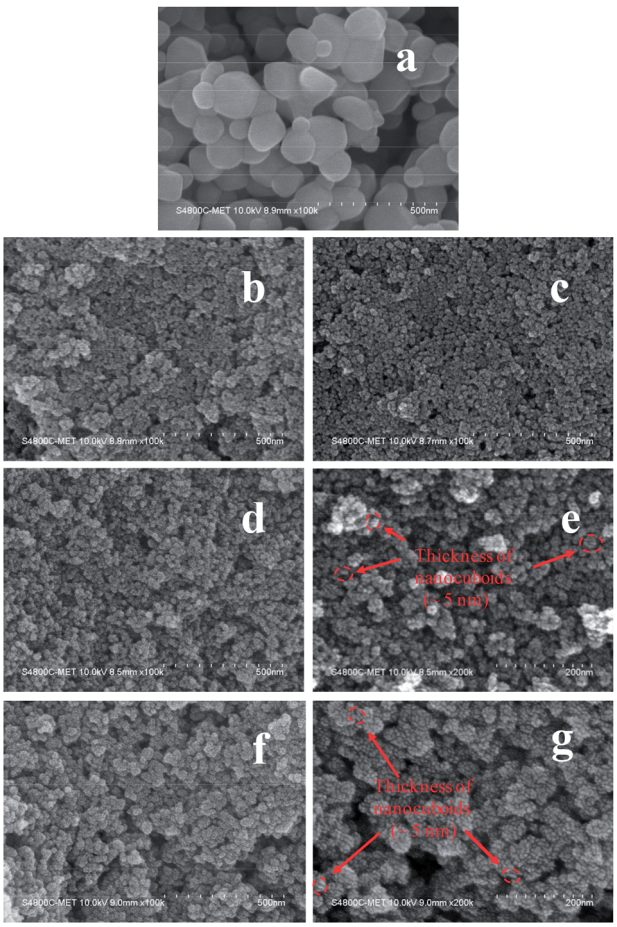

Fig. 3 FE-SEM images of (a) commercial TiO_2 and TiO_2 nanocuboids prepared under different reaction time and temperature conditions: (b) 24 h, 200 °C; (c) 48 h, 150 °C; (d and e) 48 h, 180 °C and (f and g) 48 h, 200 °C.

clearly determined from Fig. 3b–d and f. However, slightly high-magnification FESEM images (Fig. 3e and g) distinctly shows that the TiO_2 nanostructures are composed of cuboid-like particles having a thickness of ~5 nm (as marked in the Fig. 3e and g) and size in the range of 10–20 nm. Further, the FETEM was used to confirm the morphology and size of nanoparticles as well as to examine the crystal structure of the TiO_2 nanoparticles.

Fig. 4 shows the FETEM images, high resolution TEM (HRTEM) images and the corresponding selected area electron diffraction (SAED) patterns of the commercial TiO_2 and as prepared TiO_2 NCs. FETEM image (Fig. 4a) confirms the irregular shaped morphology of commercial TiO_2. The size of the particles is in the range of 50 to 200 nm as observed by FESEM analysis. The HRTEM image indicate an equal lattice spacing of 0.35 nm corresponding to the (101) and (−101) planes of anatase TiO_2. The selected area electron diffraction (SAED) pattern (Fig. 4c) shows single crystalline nature of commercial TiO_2 along with (101) and (−101) planes.

Fig. 4d and g shows the FETEM images of TiO_2 NCs prepared for 48 h at 150 and 200 °C respectively. FETEM images clearly show that the as prepared TiO_2 nanostructures are composed of cuboid shaped particles. However, as seen from Fig. 4d and g, the increase of the reaction temperature from 150 to 200 °C, leads to increase in the particle size range from 10–20 nm to 10–40 nm. Fig. 4e and h shows the HRTEM images of TiO_2 NCs

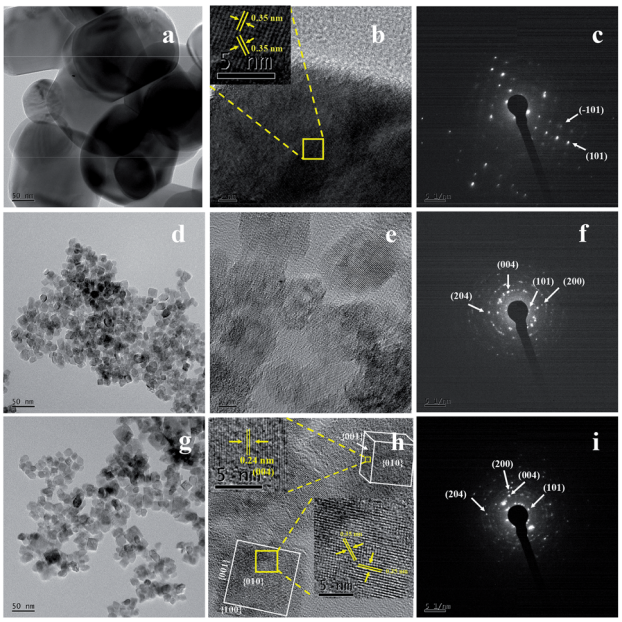

Fig. 4 FE-TEM images, HRTEM images and corresponding SAED patterns of commercial TiO_2 and as prepared TiO_2 nanocuboids: (a–c) commercial TiO_2, (d–f) TiO_2 nanocuboids prepared for 48 h at 150 °C; (g–i) TiO_2 nanocuboids prepared for 48 h at 200 °C.

prepared for 48 h at 150 and 200 °C respectively. As shown in the inset of Fig. 4h, a magnified view of the selected region of single cuboid TiO_2 nanocrystal displays visible lattice fringes with *d* spacings of 0.35 nm, which can be indexed to (101) plane of anatase TiO_2. A similar *d* spacing of 0.35 nm observed at an angle of 136.6° to (101) plane can be indexed to (−101) plane.[55] According to the crystallographic knowledge and imaging theory of TEM, the exposed facet (010) of TiO_2 is perpendicular to these two crystal facets so that TiO_2 nanocrystal is faced with {010} crystal facet, with {001} and {100} facets forming the lateral sides. Also as shown in the inset of Fig. 4h, the edge to the {010} facet is marked with *d* spacing of 0.24 nm that can be indexed to (004) planes of exposed {001} facet. This indicates that anatase TiO_2 nanocrystals are exposed with high energy {010}, {100} and {001} facets.[56,57]

The corresponding SAED patterns of the as prepared TiO_2 NCs exhibit a polycrystalline nature. The distinct diffraction rings of the SAED patterns confirm the presence of well-crystallized anatase as shown in Fig. 4f and i. The diffraction ring spots can be indexed as (101), (004), (200) and (204) crystal planes of anatase TiO_2 which is in accordance with the XRD results (Fig. 1).

3.3. XPS analysis

The X-ray photoelectron spectroscopy (XPS) analysis was performed to study the surface chemical composition of TiO_2 NCs prepared at 200 °C for 48 h and the results are presented in Fig. 5. The wide scan survey spectrum (Fig. 5a) showed that the TiO_2 NCs contain C, N, Ti, O and F elements, with photoelectron peaks appearing at binding energies of 285.82 (C 1s), 400.09 (N 1s), 458.92 (Ti 2p), 530.15 (O 1s) and 683.88 eV (F 1s) respectively.

The high-resolution C 1s spectrum (Fig. 5b) indicated one broad peak, which can be well fitted to three peaks, located at 284.58, 285.95 and 287.90 eV. The strongest peak at the binding energy of 284.58 eV corresponds to graphitic or sp^2 carbon atoms (sp^2 C=C)[58,59] and is thought to signal the presence of elemental carbon including the coke-like carbonaceous species at the surface of titania nanoparticles as well as adventitious carbon.[60,61] Whereas the peak at 285.95 eV can be assigned to sp^2 carbon–nitrogen bondings (N–sp^2 C).[58,62] The nitrogen atoms in the C–N bonds might be from the precursor or from capping agent EDTA. Further, the small peak at 287.90 eV is attributed to C=O bond[63,64] Several studies have attributed the C dopants to carbonate species present on the TiO_2 surface in the form of Ti–O=C linkages.[65] However, the absence of a peak around 281–282 eV intrinsically resulting from a Ti–C bonding (O–Ti–C linkage) indicates that carbon does not substitute the oxygen atoms in the lattice of TiO_2 (substitutional C-doping).[66] Also, no peak at around 288.6 eV suggests that there is no possibility of carbon replacing titanium atom in the lattice of TiO_2 to form a Ti–O–C structure (interstitial C-doping).[67,68] Thus, all C is adsorbed onto the surface but do not entered into the lattice of TiO_2.

Fig. 5c shows a high-resolution N 1s spectrum. After deconvolution, a single broad peak was observed at 400.21 eV

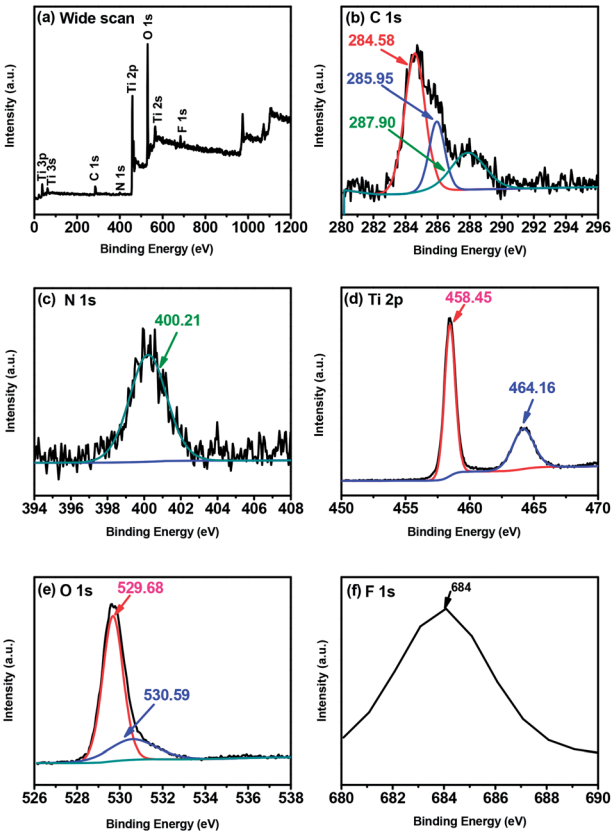

Fig. 5 XPS spectra of TiO_2 nanocuboids prepared at 200 °C for 48 h (a) the wide scan (b) C 1s, (c) N 1s, (d) Ti 2p, (e) O 1s and (f) F 1s.

which can be assigned to pyrrolic nitrogen.[69,70] In general N 1s peak around 400 eV is typically assigned to the interstitial nitrogen dopant while the peak around 396 eV is associated to the substitutional nitrogen dopant. The N 1s peak at 400.21 eV arises due to the nitrogen species bonded to oxygen sites (N–O–Ti linkage); *i.e.* an interstitial N-doping mode formed by N-atoms bonded to one or more lattice oxygen atoms. The absence of peak around 396–397 eV due to Ti–N bonding (O–Ti–N linkage) exclude the possibility of substitutional N-doping for oxygen atoms in the TiO_2 lattice.[71,72] These results indicate that N is only interstitially incorporated into the lattice of TiO_2. The origin of this N doping was either from the used NH_3 or EDTA during the synthesis of TiO_2 nanocuboids.

Fig. 5d shows the XPS spectrum of Ti 2p doublet peaks. The binding energies of Ti $2p_{3/2}$ and Ti $2p_{1/2}$ are located at approximately 458.45 eV and 464.16 eV, respectively. The splitting between the Ti $2p_{1/2}$ and Ti $2p_{3/2}$ core levels is 5.71 eV, indicating a normal state of Ti^{4+} in the TiO_2.[66,73]

As shown in Fig. 5e, the high-resolution O 1s spectrum is composed of two peaks. The major peak located at 529.68 eV is ascribed to lattice oxygen (Ti–O–Ti),[74,75] whereas the small peak centered at 530.59 eV is due to the contributions from C=O or O=C–OH.[76]

Fig. 5f shows the high-resolution XPS spectrum of the F 1s region. A single peak observed around 684 eV is due to the surface fluoride (≡Ti–F) formed by ligand exchange reaction

between F^- and the surface hydroxyl group on the surface of TiO_2.[77,78] TiO_2 sample exhibited this peak, despite being washed the titanic acid precipitate several times with distilled water (and additionally with ethanol), indicating that the F^- ions (from HF) are bound to the surface. The peak around 688.5 eV is not observed indicating the absence of F^- ions in the lattice of TiO_2.[77,79] This indicates that F is only adsorbed on the surface of TiO_2.

The overall XPS results indicate that the C and F are adsorbed on the surface of TiO_2 whereas N is doped at the interstitial sites of TiO_2 lattice.

The shift of the (101) XRD peak toward lower 2θ value may be due to the presence of Ti–O–N–O linkages formed by interstitial doping of nitrogen in the lattice of TiO_2. The presence of oxidized nitrogen is due to the nitrogen substitution for titanium in TiO_2 lattice.[80] Hsu *et al.* reported that N chemical states of the positively charged nitrogen species (N^{2+} or N^{3+}) correspond to Ti–O–N–O linkage. Interstitial doping affects the lattice structure of N-doped TiO_2.[81]

3.4. FTIR analysis

Fourier transform infrared (FTIR) spectra of commercial TiO_2 and TiO_2 NCs prepared at 200 °C for 48 h are shown in Fig. S1 (ESI†). The bands located from 400–1000 cm^{-1} are attributed to Ti–O stretching and Ti–O–Ti bridging stretching modes. A broad band observed in between 3000–3600 cm^{-1} is due to the O–H stretching mode of hydroxyl group. The band at 1659 cm^{-1} for TiO_2 Ncs prepared at 200 °C for 48 h can be attributed to the O=C–O–Ti bond of the carbonate structure, further confirming that doped carbon substituted surface Ti atoms to form a carbonate structure, while the band at 1645 cm^{-1} for commercial TiO_2 is due to the O–H bending vibrations of the adsorbed water molecules.[82,83]

The band at 1535 cm^{-1} is assigned to the N–H in-plane bending vibration and C–N stretching vibration and the band at 1179 cm^{-1} is due to C–N stretching.[84] No such nitrogen related bands are observed for commercial TiO_2, suggesting that the N species have been incorporated into the lattice of TiO_2 nanocuboids.

3.5. UV-visible-DRS spectra

The UV-vis diffuse reflectance spectra of commercial TiO_2 and as prepared TiO_2 NCs are shown in Fig. 6a. The commercial TiO_2 shows the typical optical absorption in the UV part of the spectrum whereas all of the as prepared TiO_2 NCs show higher UV absorption intensity with a distinct new absorption tail in the visible light region (400–750 nm). Park *et al.*[79] have been reported that surface fluoride species are responsible for higher UV absorption whereas the absorption edge region is unaffected by the surface fluorination when F–TiO_2 is prepared around pH 3–4. However the enhanced absorption in the visible region (the tail) could be attributed to the interstitial N-doping as reported in the previous article[61] as well as the presence of carbonaceous and carbonate species on the surface of TiO_2 NCs. The carbonaceous and carbonate species can act as a photosensitizer and could cause a long-tailed absorption in the visible-light region.[65,85–87] Thus TiO_2 NCs can absorb more number of photons and can increase the number of photogenerated

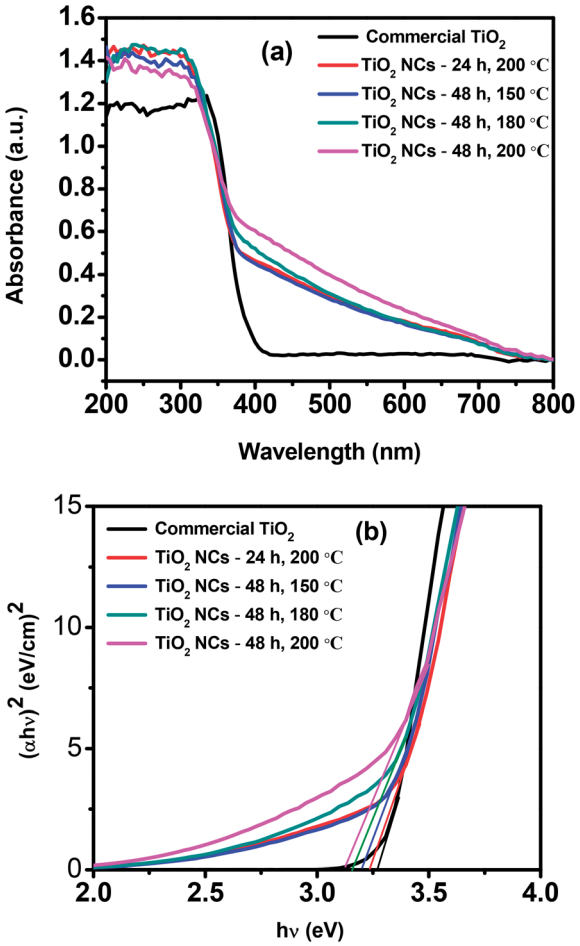

Fig. 6 (a) UV-visible diffuse reflectance spectra and (b) Tauc plots of commercial TiO_2 and as prepared TiO_2 nanocuboids.

electrons and holes to participate in the photocatalytic reaction. All these would enhance the photocatalytic activity of TiO_2 NCs.

Band gap energies (E_g) of the commercial TiO_2 and as prepared TiO_2 NCs can be estimated by using Tauc plots. Fig. 6b shows the plot of $(\alpha h\nu)^2$ *versus* $h\nu$, where α is the absorption coefficient and $h\nu$ is the photon energy. The intercept of the tangent to the X axis gives the bandgap value. The band gap of commercial TiO_2 was found to be 3.27 eV and for TiO_2 NCs prepared at different reaction conditions, *i.e.* 24 h, 200 °C; 48 h, 150 °C; 48 h, 180 °C and 48 h, 200 °C, the band gap values were 3.24, 3.20, 3.16 and 3.12 eV respectively (Table 1).

It has been reported that, surface carbonaceous and carbonate species as well as interstitial nitrogen species (Ti–O–N) may not cause significant change of TiO_2 band gap.[60,65,88] In the present report also, as compared to the band gap of commercial TiO_2, there was no considerable decrease of the band gap for as prepared TiO_2 NCs and the band gap values are slightly lower than commercial TiO_2.

3.6. BET surface areas

The Brunauer–Emmett–Teller specific surface areas (S_{BET}) of the commercial TiO_2 and TiO_2 NCs are listed in Table 1. The

specific surface area of commercial TiO_2 powder was measured about 29.3 $m^2 g^{-1}$. The measured surface areas of the TiO_2 NCs prepared at different reaction conditions *i.e.* 24 h, 200 °C; 48 h, 150 °C; 48 h, 180 °C and 48 h, 200 °C were 122.9, 111.6, 103.2 and 85.7 $m^2 g^{-1}$ respectively. As can be seen from Table 1, the BET surface areas of the as prepared TiO_2 NCs decrease with the increase of reaction time and temperature.

Fig. S2† shows the nitrogen adsorption–desorption isotherms and their corresponding pore size distributions of commercial TiO_2 and as prepared TiO_2 NCs. As shown in the Fig. S2a (ESI†), all of the samples exhibited isotherm of type IV (Brunauer–Deming–Deming–Teller (BDDT) classification) at relative pressure range of 0.7–1.0, associated with capillary condensation of gases within mesopores (2–50 nm). The isotherms show high adsorption at high relative pressure approaching 1.0, indicating the formation of large mesopores. Commercial TiO_2 has lowest N_2 volume adsorption indicating lower surface area as compared to other prepared TiO_2 NCs. With increasing hydrothermal time and temperature, the hysteresis loops gradually became smaller with decrease in surface area of TiO_2 NCs. The hysteresis loop is of type H3, which is consistent with slit shaped pores resulted from aggregates of plate-like particles.[89] Since the TiO_2 nanocrystals themselves do not have any mesopores, these mesopores could be attributed to the aggregation of nanocrystals. These kind of organized porous structures might be useful in photocatalysis as they possess efficient transport pathways to reactant and product molecules. The corresponding pore size distribution of the samples is shown in Fig. S2b (ESI†). The pore size distribution of the samples is calculated from desorption branch of the nitrogen isotherm using the BJH (Barrett–Joyner–Halenda) method. Specific surface area, pore volume and average pore size of commercial TiO_2 and as prepared TiO_2 NCs are listed in Table S1 (ESI†). With rise in reaction time and temperature, the decrease of specific surface area is observed for TiO_2 NCs. This may be due to the growth and coarsening of TiO_2 NCs during the synthesis process.

3.7. Formation mechanism of the TiO_2 nanocuboids

The possible mechanism for the formation of TiO_2 NCs is illustrated in Fig. 7. Commercial titanium(IV) oxide first react with hydrogen fluoride to produce dihydrogen hexafluorotitanate (hydroflurotitanic acid, H_2TiF_6)[90] and water which is then neutralized with aqueous ammonia to give hydrated titanium oxide *i.e.* titanic acid (H_2TiO_3) as shown in eqn (S1) and (S2) (ESI†). When $TiO_2(H_2O)$ *i.e.* H_2TiO_3 (titanic acid) reacts with hydrogen peroxide and ammonia, ammonium peroxotitanate complex is formed[91] (eqn (S3)) (ESI†). This complex on further treatment with ethylenediamine tetraacetic acid (EDTA), forms ammonium peroxotitanate EDTA complex (eqn (S4)) (ESI†). Under hydrothermal condition this complex slowly decomposes and releases O_2 to form TiO_2 (eqn (S5)) (ESI†).

Initially, tiny nuclei of TiO_2 are produced in the supersaturated solution and further growth of nanoparticles take place with time. The newly formed TiO_2 nanoparticles are spontaneously aggregated to minimize their surface energy. Here EDTA, prevents the agglomeration of TiO_2 nanoparticles and controls their shape and morphology resulting in smaller sized particles. These nanoparticles further grow anisotropically along the 3D direction resulting in the formation of cuboid-like morphology.

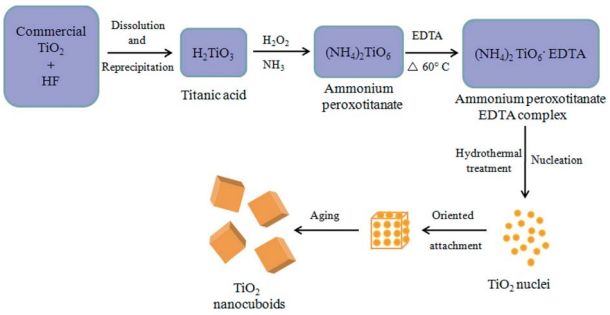

Fig. 7 A proposed mechanism for the formation of TiO_2 nanocuboids.

3.8. Photocatalytic hydrogen generation

The photocatalytic performance of the commercial TiO_2 and as prepared TiO_2 NCs was evaluated with the photocatalytic hydrogen generation from water under UV-visible light irradiation. As shown in Fig. 8, the commercial TiO_2 sample exhibited lowest H_2 evolution activity that 3325.22 μmol of H_2 was generated in 4 h. However, TiO_2 NCs prepared under different reaction time and temperature conditions showed enhanced photocatalytic H_2 generation activity.

The cumulative amounts of H_2 evolved in 4 h were 6825.62, 7697.26, 11 819.12 and 15 465.78 μmol for the TiO_2 NCs prepared for 24 h at 200 °C, 48 h at 150 °C, 48 h at 180 °C and 48 h at 200 °C respectively. Hydrogen generation rates of commercial and as prepared TiO_2 NCs are summarized in Table 1. The higher photocatalytic activity of as prepared TiO_2 NCs is due to the high specific surface areas in the range of 85.7–122.9 $m^2 g^{-1}$, much higher than that of commercial anatase TiO_2 (29.3 $m^2 g^{-1}$).

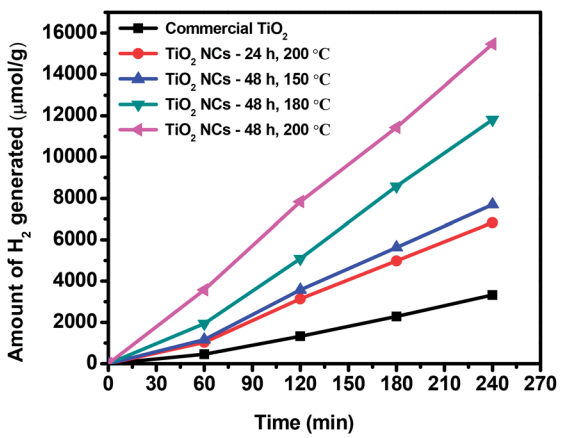

Fig. 8 Cumulative amount of hydrogen generated from the commercial TiO_2 and TiO_2 nanocuboids in 4 h of irradiation.

It is known that the photocatalytic performance of the photocatalyst depends on the two key factors, specific surface area and crystallinity. Photocatalysts with a high specific surface area offers a higher number of active sites and can provide short diffusion distances for electrons and holes to get to the surface active sites, thus limiting the recombination probability.[92] From Table 1 it can be observed that, among all of the as prepared TiO_2 NCs, NCs prepared at 200 °C for 48 h displays the smallest specific surface area *i.e.* 85.7 $m^2\ g^{-1}$ but demonstrates the best photocatalytic activity than the TiO_2 NCs prepared at same temperature for 24 h and having higher specific surface area, *i.e.* 122.9 $m^2\ g^{-1}$. This is due to the slightly high relative crystallinity of the TiO_2 NCs prepared at 200 °C for 48 h. If the crystallinity is high, the charge carriers can reach the surface without getting trapped by the defects (that act as recombination centers of photogenerated carriers) which is helpful for enhancement of photocatalytic activity. The photoluminescence (PL) study can provide useful information about the efficiency of electron–hole recombination. The PL emission spectra of the prepared TiO_2 NCs with an excitation wavelength of 275 nm are presented in ESI as Fig. S3.† The single PL emission peaks centered around 364 nm indicate the formation of defect free TiO_2 nanostructures. It is well reported that, higher emission peak intensity signifies higher recombination of photogenerated charge carriers which results in lowering of photocatalytic activity.[53,73] In our case, the same trend is observed *i.e.* TiO_2 NCs prepared at 200 °C for 24 h showed higher emission peak intensity and lower photocatalytic activity, whereas the TiO_2 NCs prepared at 200 °C for 48 h showed lower emission peak intensity and higher photocatalytic activity. Additionally, the good crystallinity observed in TiO_2 NCs prepared at 200 °C for 48 h is also responsible for higher photocatalytic activity because the crystallinity plays an important role than specific surface area in enhancing the photocatalytic activity.

In addition to the large surface area and high crystallinity, good light absorption capacity of photocatalysts and efficient charge separation of photogenerated electrons and holes also contribute to the high photocatalytic activity. All of the as prepared TiO_2 NCs exhibited higher photocatalytic H_2 generation efficiency in contrast to the commercial TiO_2 because of the improved light response in the range of 400–750 nm. We have used platinum (Pt) as a co-catalyst and methanol as a sacrificial reagent during the photocatalytic experiments to suppress the electron–hole recombination. Moreover, it has also been reported that surface fluorination can also greatly reduce the recombination of photogenerated electron–hole pairs, as surface ≡Ti–F groups can act as electron-trapping sites retaining photogenerated electrons due to the strong electronegativity of the fluoride. Thus, more efficient charge separation will be produced, leading therefore to the enhancement of the photocatalytic activity.[11,75,76]

Fig. 9 illustrates the mechanism of photocatalytic H_2 generation from water. When TiO_2 nanocuboid absorbs a photon with energy equal to or greater than its band gap, electrons are excited from the valence band (VB) to the conduction band (CB) leaving the holes in the VB. The photo-excited electrons and holes can migrate to the surface of the TiO_2. Electron–hole pairs that reach the surface without recombination, participate in the photocatalytic reactions of water splitting. Use of Pt as a co-catalyst and methanol as a sacrificial reagent helps to reduce the recombination of electrons and holes. As the bottom edge of the conduction band (CB) of TiO_2 is more negative than the H_2 evolution level (EH_2/H_2O), and the top edge of the valence band (VB) is more positive than the oxygen generation level (EH_2O/O_2), photoinduced electrons and holes react with the water adsorbed on the surface of TiO_2. As a result, H^+ is reduced into H_2 and H_2O is oxidized into O_2.[93,94]

As discussed earlier and as shown in Table 1, the hydrogen evolution rate of the TiO_2 NCs prepared at 200 °C for 48 h (3866.44 μmol $h^{-1}\ g^{-1}$) is much higher than that of commercial TiO_2 (831.30 μmol $h^{-1}\ g^{-1}$). This 4.65-fold increase in the photocatalytic activity of TiO_2 NCs can be ascribed to the synergistic effect of high specific surface area, good crystallinity, enhanced light absorption in the range of 400–750 nm and effective separation of electron–hole pairs. This reported H_2 generation rate is also high as compared to the previous reports. Table S2 (ESI†) provides comparison of the H_2 generation activity of previously reported different anatase TiO_2 nanostructures with the anatase TiO_2 NCs presented in this work.

In order to evaluate the stability and the reusability of the catalyst, a recycling study of the most active sample *i.e.* TiO_2 NCs prepared at 200 °C for 48 h was carried out in terms of its photocatalytic hydrogen production. The same catalyst was recycled three times in the hydrogen generation reactions (Fig. 10). It is observed that the catalytic activity of TiO_2 NCs did not exhibit any significant loss in the second and third cycles. After third cycle, the amount of H_2 generated is around 14 770 μmol of H_2, per g of recycled catalyst (*i.e.* 3692.50 μmol $h^{-1}\ g^{-1}$), indicating the high stability of the catalyst towards hydrogen generation.

To support higher photocatalytic activity of TiO_2 NCs prepared at 200 °C for 48 h, the photoconductivity measurements of all prepared TiO_2 NCs were carried out and compared with commercial TiO_2.

3.9. Photoconductivity measurements

Photoconductivity measurements were carried out as per our previous report.[95] Fig. S4 (ESI†) shows *I–V* characteristics for

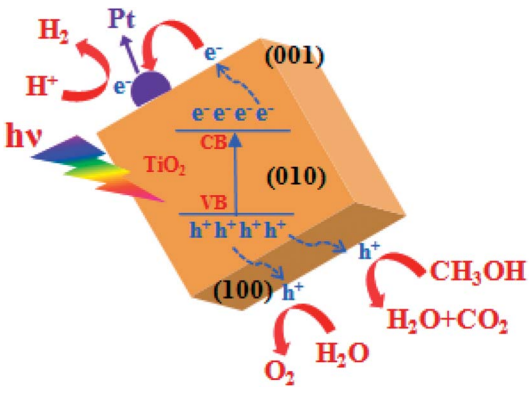

Fig. 9 Schematic illustration of the mechanism of photocatalytic H_2 generation from water over TiO_2 nanocuboid.

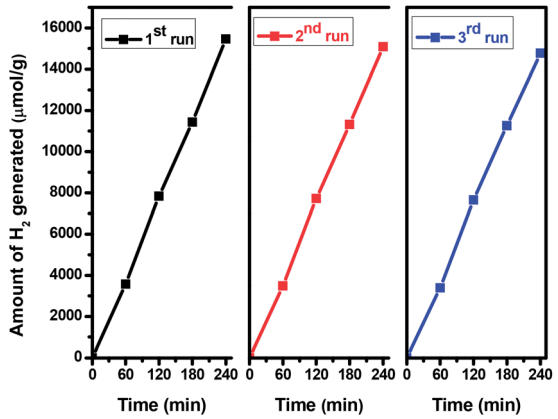

Fig. 10 Recyclability of the hydrogen generation behavior of TiO_2 nanocuboids prepared at 200 °C for 48 h.

commercial TiO_2 and as prepared TiO_2 NCs using two probes with applied bias voltage from −5 V to +5 V under illumination of light. *I–V* measurements were carried out under 1000 W xenon lamp and 1.5 (air-mass ratio). As can be seen from the inset of the figure, commercial TiO_2 shows less response to photocurrent as compared to prepared TiO_2 NCs. However photocurrent response increases as increase in the time and temperature conditions of TiO_2 NCs. The highest photocurrent was observed for TiO_2 NCs prepared at 200 °C for 48 h. The two order enhanced photocurrent clearly correlate the enhanced photocatalytic performance of TiO_2 NCs prepared at 200 °C for 48 h as compared to other TiO_2 NCs. This may be due to better crystallinity attributing higher photocatalytic performance as compared to other TiO_2 NCs. In nutshell, the enhanced hydrogen evolution is due to nanostructuring of material along with good crystallinity.

4. Conclusions

Commercial anatase TiO_2 was successfully modified into highly crystalline 3D NCs *via* hydrothermal method at different reaction time and temperature conditions. TiO_2 NCs prepared at different time and temperature conditions found to have high specific surface area as compared to the commercial TiO_2. As prepared TiO_2 NCs were explored for hydrogen production from photocatalytic water splitting. Obvious enhancement in the photocatalytic performance of the TiO_2 NCs was demonstrated in H_2 production, compared to the commercial TiO_2. TiO_2 NCs obtained at 200 °C for 48 h exhibited the highest photocatalytic H_2 generation rate (3866.44 μmol h^{-1} g^{-1}), which is 4.65 times higher than that of commercial TiO_2. Also, TiO_2 NCs exhibited the good cycling stability. The enhanced photocatalytic activity of TiO_2 NCs obtained at 200 °C for 48 h as compared to commercial TiO_2 could be attributed to its large specific surface area, good crystallinity, extended visible light absorption and efficient separation of photo-induced carriers. The photoconductive study supports the higher photocatalytic performance of TiO_2 NCs prepared at 200 °C for 48 h. This study provides a simple and economical way to prepare highly active and promising anatase TiO_2 photocatalyst for hydrogen generation from water.

Conflicts of interest

There are no conflicts to declare.

Acknowledgements

Authors are grateful to Director, C-MET, Pune for providing the necessary characterization facility and for useful discussion. The authors are grateful to Ministry of Electronics and Information Technology (MeitY), Govt. of India, New Delhi for financial support.

Notes and references

1 M. Humayun, F. Raziq, A. Khan and W. Luo, Modification strategies of TiO_2 for potential applications in photocatalysis: a critical review, *Green Chem. Lett. Rev.*, 2018, **11**, 86–102.
2 Z. Bian, T. Tachikawa, P. Zhang, M. Fujitsuka and T. Majima, Au/TiO_2 Superstructure-Based Plasmonic Photocatalysts Exhibiting Efficient Charge Separation and Unprecedented Activity, *J. Am. Chem. Soc.*, 2014, **136**, 458–465.
3 H. Huang, C. Wang, J. Huang, X. Wang, Y. Du and P. Yang, Structure inherited synthesis of N-doped highly ordered mesoporous Nb_2O_5 as robust catalysts for improved visible light photoactivity, *Nanoscale*, 2014, **6**, 7274–7280.
4 Y. Li, Y.-K. Peng, L. Hu, J. Zheng, D. Prabhakaran, S. Wu, T. J. Puchtler, M. Li, K.-Y. Wong, R. A. Taylor and S. C. E. Tsang, Photocatalytic water splitting by N-TiO_2 on MgO(111) with exceptional quantum efficiencies at elevated temperatures, *Nat. Commun.*, 2019, **10**, 4421.
5 A. Kudo and Y. Miseki, Heterogeneous photocatalyst materials for water splitting, *Chem. Soc. Rev.*, 2009, **38**, 253–278.
6 X. B. Chen, S. H. Shen, L. J. Guo and S. S. Mao, Semiconductor-based Photocatalytic Hydrogen Generation, *Chem. Rev.*, 2010, **110**, 6503–6570.
7 A. Fujishima and K. Honda, Electrochemical Photolysis of Water at a Semiconductor Electrode, *Nature*, 1972, **238**, 37–38.
8 W. Y. Teoh, J. A. Scott and R. Amal, Progress in Heterogeneous Photocatalysis: From Classical Radical Chemistry to Engineering Nanomaterials and Solar Reactors, *J. Phys. Chem. Lett.*, 2012, **3**, 629–639.
9 A. O. Ibhadon and P. Fitzpatrick, Heterogeneous Photocatalysis: Recent Advances and Applications, *Catalysts*, 2013, **3**, 189–218.
10 G. L. Chiarello, M. V. Dozzi and E. Selli, TiO_2-based materials for photocatalytic hydrogen production, *J. Energy Chem.*, 2017, **26**, 250–258.
11 S. Kansal, P. Kundu, S. Sood, R. Lamba, A. Umar and S. K. Mehta, Photocatalytic degradation of antibiotic levofloxacin using well-crystalline TiO_2 nanoparticles, *New J. Chem.*, 2014, **38**, 3220–3226.

12 Y. Wang, C. Sun, X. Zhao, B. Cui, Z. Zeng, A. Wang, G. Liu and H. Cui, The Application of Nano-TiO_2 Photo Semiconductors in Agriculture, *Nanoscale Res. Lett.*, 2016, **11**, 529.

13 V. Kumaravel, S. Mathew, J. Bartlett and S. C. Pillai, Photocatalytic hydrogen production using metal doped TiO_2: A review of recent advances, *Appl. Catal., B*, 2019, **244**, 1021–1064.

14 S. Ge, D. Li, G. Jia, B. Wang, Z. Yang, Z. Yang, H. Qiao, Y. Zhang and Z. Zheng, Hydrofluoric Acid Controlled TiO_2 Phase Transformation from Rutile to Anatase at Room Temperature and Their Photocatalytic Performance, *J. Nanosci. Nanotechnol.*, 2015, **15**, 6636–6641.

15 L. Zhang, L. Tian, Y. Liu, T. Tan, D. Liu and C. Wang, Synthesis of tapered tetragonal nanorods of anatase TiO_2 with enhanced photocatalytic activity *via* a sol-hydrothermal process mediated by H_2O_2 and NH_3, *J. Mater. Chem. A*, 2015, **3**, 15265–15273.

16 L. Chen, Q. Gu, L. Hou, C. Zhang, Y. Lu, X. Wang and J. Long, Molecular p–n heterojunction-enhanced visible-light hydrogen evolution over N-doped TiO_2 photocatalyst, *Catal. Sci. Technol.*, 2017, **7**, 2039–2049.

17 M. Ismael, Highly effective ruthenium-doped TiO_2 nanoparticles photocatalyst for visible-light-driven photocatalytic hydrogen production, *New J. Chem.*, 2019, **43**, 9596–9605.

18 N. Vinothkumar and M. De, Enhanced photocatalytic hydrogen production from water methanol mixture using cerium and nonmetals (B/C/N/S) co-doped titanium dioxide, *Mater. Renew. Sustain. Energy*, 2014, **3**, 25.

19 Y. Yang, D. Ni, Y. Yao, Y. Zhong, Y. Ma and J. Yao, High photocatalytic activity of carbon doped TiO_2 prepared by fast combustion of organic capping ligands, *RSC Adv.*, 2015, **5**, 93635–93643.

20 M. Murdoch, G. I. N. Waterhouse, M. A. Nadeem, J. B. Metson, M. A. Keane, R. F. Howe, J. Llorca and H. Idriss, The effect of gold loading and particle size on photocatalytic hydrogen production from ethanol over Au/TiO_2 nanoparticles, *Nat. Chem.*, 2011, **3**, 489–492.

21 J. M. Valero, S. Obregón and G. Colon, Active Site Considerations on the Photocatalytic H_2 Evolution Performance of Cu-Doped TiO_2 Obtained by Different Doping Methods, *ACS Catal.*, 2014, **4**, 3320–3329.

22 M.-C. Wu, A. Sapi, A. Avila, M. Szabo, J. Hiltunen, M. Huuhtanen, G. Toth, A. Kukovecz, Z. Konya, R. Keiski, W.-F. Su, H. Jantunen and K. Kordas, Enhanced Photocatalytic Activity of TiO_2 Nanofibers and Their Flexible Composite Films: Decomposition of Organic Dyes and Efficient H_2 Generation from Ethanol–Water Mixtures, *Nano Res.*, 2011, **4**, 360–369.

23 A. M. Hussein, L. Mahoney, R. Peng, H. Kibombo, C.-M. Wu, R. T. Koodali and R. Shende, Mesoporous coupled ZnO/TiO_2 photocatalyst nanocomposites for hydrogen generation, *J. Renewable Sustainable Energy*, 2013, **5**, 033118.

24 J. Fang, L. Xu, Z. Zhang, Y. Yuan, S.-W. Cao, Z. Wang, L. Yin, Y. Liao and C. Xue, Au@TiO_2-CdS Ternary Nanostructures for Efficient Visible-light-Driven Hydrogen Generation, *ACS Appl. Mater. Interfaces*, 2013, **5**, 8088–8092.

25 Y. Lin, P. Ren and C. Wei, Fabrication of MoS_2/TiO_2 heterostructure with enhanced photocatalytic activity, *CrystEngComm*, 2019, **21**, 3439–3450.

26 Y. Yamazaki, K. Azami, R. Katoh and S. Yamazaki, Developing Active TiO_2 Nanorods by Examining the Influence of Morphological Changes from Nanorods to Nanoparticles on Photocatalytic Activity, *ACS Appl. Nano Mater.*, 2018, **1**, 5927–5935.

27 M. Shahrezaei, S. Habibzadeh, A. A. Babaluo, H. Hosseinkhani, M. Haghighi, A. Hasanzadeh and R. Tahmasebpour, Study of synthesis parameters and photocatalytic activity of TiO_2 nanostructures, *J. Exp. Nanosci.*, 2017, **12**, 45–61.

28 Y. Du, W. Li, Y. Bai, Z. Huangfu, W. Wang, R. Chai, C. Chen, X. Yang and Q. Feng, Facile synthesis of TiO_2/Ag_3PO_4 composites with co-exposed high-energy facets for efficient photodegradation of rhodamine B solution under visible light irradiation, *RSC Adv.*, 2020, **10**, 24555–24569.

29 Y. Du, X. Niu, J. He, L. Liu, Y. Liu, C. Chen, X. Yang and Q. Feng, Hollow Square RodLike Microtubes Composed of Anatase Nanocuboids with Coexposed {100}, {010}, and {001} Facets for Improved Photocatalytic Performance, *ACS Omega*, 2020, **5**, 14147–14156.

30 O. Sacco, Di. Sannino, M. Matarangolo and V. Vaiano, Room Temperature Synthesis of V-Doped TiO_2 and Its Photocatalytic Activity in the Removal of Caffeine under UV Irradiation, *Materials*, 2019, **12**, 911.

31 D. He and F. Lin, Preparation and photocatalytic activity of anatase TiO_2 nanocrystallites with high thermal stability, *Mater. Lett.*, 2007, **61**, 3385–3387.

32 R. Acharya, B. Naik and K. Parida, Cr(VI) remediation from aqueous environment through modified-TiO_2-mediated photocatalytic reduction, *Beilstein J. Nanotechnol.*, 2018, **9**, 1448–1470.

33 K. Zimny, T. Roques-Carmes, C. Carteret, M. J. Stebe and J. L. Blin, Synthesis and Photoactivity of Ordered Mesoporous Titania with a Semicrystalline Framework, *J. Phys. Chem. C*, 2012, **116**, 6585–6594.

34 Y.-F. Li and Z.-P. Liu, Particle Size, Shape and Activity for Photocatalysis on Titania Anatase Nanoparticles in Aqueous Surroundings, *J. Am. Chem. Soc.*, 2011, **133**, 15743–15752.

35 H. Yang, K. Zhang, R. Shi, X. Li, X. Dong and Y. Yu, Sol–gel synthesis of TiO_2 nanoparticles and photocatalytic degradation of methyl orange in aqueous TiO_2 suspensions, *J. Alloys Compd.*, 2006, **413**, 302–306.

36 S. Lee, I.-S. Cho, J. H. Lee, D. H. Kim, D. W. Kim, J. Y. Kim, H. Shin, J.-K. Lee, H. S. Jung, N.-G. Park, K. Kim, M. J. Ko and K. S. Hong, Two-Step Sol-Gel Method-Based TiO_2 Nanoparticles with Uniform Morphology and Size for Efficient Photo-Energy Conversion Devices, *Chem. Mater.*, 2010, **22**, 1958–1965.

37 J.-N. Nian and H. Teng, Hydrothermal Synthesis of Single-Crystalline Anatase TiO_2 Nanorods with Nanotubes as the Precursor, *J. Phys. Chem. B*, 2006, **110**, 4193–4198.

38 X. Niu, Y. Du, Y. Liu, H. Qi, J. An, X. Yang and Q. Feng, Hydrothermal synthesis and formation mechanism of the

anatase nanocrystals with co-exposed high energy {001}, {010} and [111]-facets for enhanced photocatalytic performance, *RSC Adv.*, 2017, **7**, 24616–24627.

39 A. Jena, R. Vinu, S. A. Shivashankar and G. Madras, Microwave Assisted Synthesis of Nanostructured Titanium Dioxide with High Photocatalytic Activity, *Ind. Eng. Chem. Res.*, 2010, **49**, 9636–9643.

40 Y. Chimupala, G. Hyett, R. Simpson, R. Mitchell, R. Douthwaite, S. J. Milne and R. D. Brydson, Synthesis and characterization of mixed phase anatase TiO_2 and sodium-doped TiO_2(B) thin films by low pressure chemical vapour deposition (LPCVD), *RSC Adv.*, 2014, **4**, 48507–48515.

41 M. Dhiman, R. Sharma, V. Kumar and S. Singhal, Morphology controlled hydrothermal synthesis and photocatalytic properties of $ZnFe_2O_4$ nanostructures, *Ceram. Int.*, 2016, **42**, 12594–12605.

42 H. Yin, G. Ding, B. Gao, F. Huang, X. Xie and M. Jiang, Synthesis of ultrafine titanium dioxide nanowires using hydrothermal method, *Mater. Res. Bull.*, 2012, **47**, 3124–3128.

43 K. C. Sun, M. B. Qadir and S. H. Jeong, Hydrothermal synthesis of TiO_2 nanotubes and their application as an over-layer for dye-sensitized solar cells, *RSC Adv.*, 2014, **4**, 23223–23230.

44 P. Hu, G. Du, W. Zhou, J. Cui, J. Lin, H. Liu, D. Liu, J. Wang and S. Chen, Enhancement of Ethanol Vapor Sensing of TiO_2 Nanobelts by Surface Engineering, *ACS Appl. Mater. Interfaces*, 2010, **2**, 3263–3269.

45 K. Santhi, M. Navaneethan, S. Harish, S. Ponnusamy and C. Muthamizhchelvan, Synthesis and characterization of TiO_2 nanorods by hydrothermal method with different pH conditions and their photocatalytic activity, *Appl. Surf. Sci.*, 2020, **500**, 144058.

46 W. Zhang, Y. Xie, D. Xiong, X. Zeng, Z. Li, M. Wang, Y.-B. Cheng, W. Chen, K. Yan and S. Yang, TiO_2 Nanorods: A Facile Size- and Shape-Tunable Synthesis and Effective Improvement of Charge Collection Kinetics for Dye-Sensitized Solar Cells, *ACS Appl. Mater. Interfaces*, 2014, **6**, 9698–9704.

47 X. Han, Q. Kuang, M. Jin, Z. Xie and L. Zheng, Synthesis of Titania Nanosheets with a High Percentage of Exposed (001) Facets and Related Photocatalytic Properties, *J. Am. Chem. Soc.*, 2009, **131**, 3152–3153.

48 C. Wang, L. Yin, L. Zhang, Y. Qi, N. Lun and N. Liu, Large Scale Synthesis and Gas-Sensing Properties of Anatase TiO_2 Three-Dimensional Hierarchical Nanostructures, *Langmuir*, 2010, **26**, 12841–12848.

49 T. Zhu, J. Li and Q. Wu, Construction of TiO_2 Hierarchical Nanostructures from Nanocrystals and Their Photocatalytic Properties, *ACS Appl. Mater. Interfaces*, 2011, **3**, 3448–3453.

50 Y. Yang, J. X. Hu, Y. Liang, J. P. Zou, K. Xu, R. J. Hu, Z. D. Zou, Q. Yuan, Q. Q. Chen, Y. Lu, T. Yu and C. L. Yuan, Anatase TiO_2 hierarchical microspheres consisting of truncated nanothorns and their structurally enhanced gas sensing performance, *J. Alloys Compd.*, 2017, **694**, 292–299.

51 J. Yu, L. Qi and M. Jaroniec, Hydrogen Production by Photocatalytic Water Splitting over Pt/TiO_2 Nanosheets with Exposed (001) Facets, *J. Phys. Chem. C*, 2010, **114**, 13118–13125.

52 J. Jitputti, T. Rattanavoravipa, S. Chuangchote, S. Pavasupree, Y. Suzuki and S. Yoshikawa, Low temperature hydrothermal synthesis of monodispersed flower-like titanate nanosheets, *Catal. Commun.*, 2009, **10**, 378–382.

53 G. Cheng, Y. Wei, J. Xiong, Y. Gan, J. Zhu and F. Xu, Same titanium glycolate precursor but different products: Successful synthesis of twinned anatase TiO_2 nanocrystals with excellent solar photocatalytic hydrogen evolution capability, *Inorg. Chem. Front.*, 2017, **4**, 1319–1329.

54 S. Ida, P. Wilson, B. Neppolian, M. Sathish, P. Karthik and P. Ravi, Ultrasonically aided selective stabilization of pyrrolic type nitrogen by one pot nitrogen doped and hydrothermally reduced Graphene oxide/Titania nanocomposite (N-TiO_2/N-RGO) for H_2 production, *Ultrason. Sonochem.*, 2019, **57**, 62–72.

55 B. Wu, C. Guo, N. Zheng, Z. Xie and G. D. Stucky, Nonaqueous Production of Nanostructured Anatase with High-Energy Facets, *J. Am. Chem. Soc.*, 2008, **130**, 17563–17567.

56 N. T. Padmanabhan, P. Ganguly, S. C. Pillai and H. John, Morphology engineered spatial charge separation in superhydrophilic TiO_2/graphene hybrids for hydrogen production, *Mater. Today Energy*, 2020, **17**, 100447.

57 Q. Huang, S. Tian, D. Zeng, X. Wang, W. Song, Y. Li, W. Xiao and C. Xie, Enhanced photocatalytic activity of chemically bonded TiO_2/graphene composites based on the effective interfacial charge transfer through C-Ti bond, *ACS Catal.*, 2013, **3**, 1477–1485.

58 T. Hu, X. Sun, H. Sun, G. Xin, D. Shao, C. Liu and J. Lian, Rapid Synthesis of Nitrogen-Doped Graphene for Lithium ion Battery Anode with Excellent Rate Performance and Super-long Cyclic Stability, *Phys. Chem. Chem. Phys.*, 2014, **16**, 1060–1066.

59 Y. Dong, H. Pang, H. B. Yang, C. Guo, J. Shao, Y. Chi, C. M. Li and T. Yu, Carbon-Based Dots Co-doped with Nitrogen and Sulfur for High Quantum Yield and Excitation-Independent Emission, *Angew. Chem., Int. Ed.*, 2013, **52**, 7800–7804.

60 G.-S. Shao, L. Liu, T.-Y. Ma, F.-Y. Wang, T.-Z. Ren and Z.-Y. Yuan, Synthesis and characterization of carbon-modified titania photocatalysts with a hierarchical meso-/macroporous structure, *Chem. Eng. J.*, 2010, **160**, 370–377.

61 A.-Y. Zhang, L.-L. Long, C. Liu, W.-W. Li and H.-Q. Yu, Chemical recycling of the waste anodic electrolyte from the TiO_2 nanotube preparation process to synthesize facet-controlled TiO_2 single crystals as an efficient photocatalyst, *Green Chem.*, 2014, **16**, 2745–2753.

62 W. Zhu, H. Song, L. Zhang, Y. Weng, Y. Su and Y. Lv, Fabrication of Fluorescent Nitrogen-Rich Graphene Quantum Dots by Tin (IV) Catalytic Carbonization of Ethanolamine, *RSC Adv.*, 2015, **5**, 60085–60089.

63 J. Guo, Y. Shi, H. Zhou, X. Wang and T. Ma, A novel composite of $W_{18}O_{49}$ nanorods on reduced graphene oxide sheets based on *in situ* synthesis and catalytic performance for oxygen reduction reaction, *RSC Adv.*, 2017, **7**, 2051–2057.

64 J. P. H. Li, X. Zhou, Y. Pang, L. Zhu, E. I. Vovk, L. Cong, A. P. Bavel, S. Li and Y. Yang, Understanding of binding energy calibration in XPS of lanthanum oxide by *in situ* treatment, *Phys. Chem. Chem. Phys.*, 2019, **21**, 22351–22358.

65 X. Wang, Y. Tang, M.-Y. Leiw and T.-T. Lim, Solvothermal synthesis of Fe–C codoped TiO_2 nanoparticles for visible-light photocatalytic removal of emerging organic contaminants in water, *Appl. Catal., A*, 2011, **409– 410**, 257–266.

66 N. G. Moustakas, A. G. Kontos, V. Likodimos, F. Katsaros, N. Boukos, D. Tsoutsou, A. Dimoulas, G. E. Romanos, D. D. Dionysiou and P. Falaras, Inorganic–organic core–shell titania nanoparticles for efficient visible light activated photocatalysis, *Appl. Catal., B*, 2013, **130–131**, 14–24.

67 S. K. Warkhade, G. S. Gaikwad, S. P. Zodape, U. Pratap, A. V. Maldhure and A. V. Wankhade, Low temperature synthesis of pure anatase carbon doped titanium dioxide: An efficient visible light active photocatalyst, *Mater. Sci. Semicond. Process.*, 2017, **63**, 18–24.

68 W. Ren, Z. Ai, F. Jia, L. Zhang, X. Fan and Z. Zou, Low temperature preparation and visible light photocatalytic activity of mesoporous carbon-doped crystalline TiO_2, *Appl. Catal., B*, 2007, **69**, 138–144.

69 H. Wang, T. Maiyalagan and X. Wang, Review on Recent Progress in Nitrogen-Doped Graphene: Synthesis, Characterization, and Its Potential Applications, *ACS Catal.*, 2012, **2**, 781–794.

70 F. M. Hassan, V. Chabot, J. Li, B. K. Kim, L. Ricardez-Sandoval and A. Yu, Pyrrolic-structure enriched nitrogen doped graphene for highly efficient next generation supercapacitors, *J. Mater. Chem. A*, 2013, **1**, 2904–2912.

71 C. Bittencourt, M. Rutar, P. Umek, A. Mrzel, K. Vozel, D. Arcon, K. Henzler, P. Kruger and P. Guttmann, Molecular nitrogen in N-doped TiO_2 nanoribbons, *RSC Adv.*, 2015, **5**, 23350–23356.

72 C. Yan, K.-F. Chen, C.-H. Lai, S.-W. Lai, Q. Chang and Y.-P. Peng, Photocatalytic degradation of Rhodamine B by microwave-assisted hydrothermal synthesized N-doped titanate nanotubes, *J. Environ. Sci.*, 2014, **26**, 1505–1512.

73 S. S. Thind, C. C. Mustapic, J. Wen, C. D. Goodwin and A. Chen, Facile synthesis of mesoporous carbon nitride and titanium dioxide nanocomposites with enhanced visible light photocatalytic activity, *New J. Chem.*, 2017, **41**, 10542–10549.

74 P. Zhang, C. Shao, Z. Zhang, M. Zhang, J. Mu, Z. Guo and Y. Liu, TiO_2@carbon core/shell nanofibers: Controllable preparation and enhanced visible photocatalytic properties, *Nanoscale*, 2011, **3**, 2943–2949.

75 J. C. Xu, J. J. Zhang, Z. Y. Cai, H. Huang, T. H. Huang, P. Wang and X. Y. Wang, Facile and Large-scale Synthesis of Defective Black TiO_{2-x}(B) Nanosheets for Efficient Visible-light-driven Photocatalytic Hydrogen Evolution, *Catalysts*, 2019, **9**, 1048.

76 D. Yang, A. Velamakanni, G. Bozoklu, S. Park, M. Stoller, R. D. Piner, S. Stankovich, I. Jung, D. A. Field, C. A. Ventrice Jr and R. S. Ruoff, Chemical analysis of graphene oxide films after heat and chemical treatments by X-ray photoelectron and Micro-Raman spectroscopy, *Carbon*, 2009, **47**, 145–152.

77 J. Yu, W. Wang, B. Cheng and B.-L. Su, Enhancement of Photocatalytic Activity of Mesporous TiO_2 Powders by Hydrothermal Surface Fluorination Treatment, *J. Phys. Chem. C*, 2009, **113**, 6743–6750.

78 J. J. Murcia, M. C. Hidalgo, J. A. Navio, J. Arana and J. M. Dona-Rodriguez, Study of the phenol photocatalytic degradation over TiO2modified by sulfation, fluorination, and platinum nanoparticles photodeposition, *Appl. Catal., B*, 2015, **179**, 305–312.

79 H. Park and W. Choi, Effects of TiO_2 Surface Fluorination on Photocatalytic Reactions and Photoelectrochemical Behaviors, *J. Phys. Chem. B*, 2004, **108**, 4086–4093.

80 F. Peng, L. Cai, L. Huang, H. Yu and H. Wang, Preparation of nitrogen-doped titanium dioxide with visible-light photocatalytic activity using a facile hydrothermal method, *J. Phys. Chem. Solids*, 2008, **69**, 1657–1664.

81 J.-C. Hsu, Y.-H. Lin and P. W. Wang, X-ray Photoelectron Spectroscopy Analysis of Nitrogen-Doped TiO_2 Films Prepared by Reactive-Ion-Beam Sputtering with Various NH_3/O_2 Gas Mixture Ratios, *Coatings*, 2020, **10**, 47.

82 P. Praveen, G. Viruthagiri, S. Mugundan and N. Shanmugam, Structural, optical and morphological analyses of pristine titanium di-oxide nanoparticles – Synthesized *via* sol–gel route, *Spectrochim. Acta, Part A*, 2014, **117**, 622–629.

83 C. Zhang, A. Cao, L. Chen, K. Lv, T. Wu and K. Deng, One-step topological preparation of carbon doped and coated TiO_2 hollow nanocubes for synergistically enhanced visible photodegradation activity, *RSC Adv.*, 2018, **8**, 21431–21443.

84 W. Xu, X. Yin, G. He, J. Zhao and H. Wang, Photografted temperature-sensitive poly(N-isopropylacrylamide) thin film with a superfast response rate and an interesting transparent–opaque–transparent change in its deswelling process, *Soft Matter*, 2012, **8**, 3105–3111.

85 C. Lettmann, K. Hildenbrand, H. Kisch, W. Macyk and W. F. Maier, Visible light photodegradation of 4-chlorophenol with a coke-containing titanium dioxide photocatalyst, *Appl. Catal., B*, 2001, **32**, 215–227.

86 X. Yang, C. Cao, K. Hohn, L. Erickson, R. Maghirang, D. Hamal and K. Klabunde, Highly visible-light active C- and V-doped TiO_2 for degradation of acetaldehyde, *J. Catal.*, 2007, **252**, 296–302.

87 Y.-T. Lin, C.-H. Weng, Y.-H. Lin, C.-C. Shiesh and F.-Y. Chen, Effect of C content and calcination temperature on the photocatalytic activity of C-doped TiO_2 catalyst, *Sep. Purif. Technol.*, 2013, **116**, 114–123.

88 D. Nassoko, Y.-F. Li, H. Wang, J.-L. Li, Y.-Z. Li and Y. Yu, Nitrogen-doped TiO_2 nanoparticles by using EDTA as nitrogen source and soft template: Simple preparation, mesoporous structure, and photocatalytic activity under visible light, *J. Alloys Compd.*, 2012, **540**, 228–235.

89 B. Wang, L. Guo, M. He and T. He, Green synthesis of TiO_2 nanocrystals with improved photocatalytic activity by ionic-liquid assisted hydrothermal method, *Phys. Chem. Chem. Phys.*, 2013, **15**, 9891–9898.

90 D. L. Dolcater, J. K. Syers and M. L. Jackson, Titanium As Free Oxide And Substituted Forms In Kaolinites And Other Soil Minerals, *Clays Clay Miner.*, 1970, **18**, 71–79.

91 F. Wu, X. Li, Z. Wang, L. Wu, H. Guo, X. Xiong, X. Zhang and X. Wang, Hydrogen peroxide leaching of hydrolyzed titania residue prepared from mechanically activated Panzhihua ilmenite leached by hydrochloric acid, *Int. J. Miner. Process.*, 2011, **98**, 106–112.

92 T. Jafari, E. Moharreri, A. S. Amin, R. Miao, W. Song and S. L. Suib, Photocatalytic water splitting—the untamed dream: a review of recent advances, *Molecules*, 2016, **21**, 900.

93 C.-H. Liao, C.-W. Huang and J. C. S. Wu, Hydrogen production from semiconductor-based photocatalysis *via* water splitting, *Catalysts*, 2012, **2**, 490–516.

94 M. Ni, M. K. H. Leung, D. Y. C. Leung and K. Sumathy, A review and recent developments in photocatalytic water-splitting using TiO_2 for hydrogen production, *Renewable Sustainable Energy Rev.*, 2007, **11**, 401–425.

95 S. R. Damkale, S. S. Arbuj, G. G. Umarji, R. P. Panmand, S. K. Khore, R. S. Sonawane, S. B. Rane and B. B. Kale, Two dimensional hexagonal SnS_2 nanostructures for photocatalytic hydrogen generation and dye degradation, *Sustainable Energy Fuels*, 2019, **3**, 3406–3414.